THE JOURNAL OF
PHYSICAL CHEMISTRY C

Article

pubs.acs.org/JPCC

Synthesis and Characterization of High-Photoactivity Electrodeposited Cu_2O Solar Absorber by Photoelectrochemistry and Ultrafast Spectroscopy

Adriana Paracchino,[†,*] Jan Cornelius Brauer,[†] Jacques-Edouard Moser,[†] Elijah Thimsen,[‡] and Michael Graetzel[†]

[†]Laboratory of Photonics and Interfaces, Institute of Chemical Sciences and Engineering, Ecole Polytechnique Fédérale de Lausanne, CH-1015 Lausanne, Switzerland

[‡]Argonne National Lab, Material Science Division, Argonne, Illinois 60439, United States

Ⓢ *Supporting Information*

ABSTRACT: We present a systematic study on the effects of electrodeposition parameters on the photoelectrochemical properties of Cu_2O. The influence of deposition variables (temperature, pH, and deposition current density) on conductivity has been widely explored in the past for this semiconductor, but the optimization of the electrodeposition process for the photoelectrochemical response in aqueous solutions under AM 1.5 illumination has received far less attention. In this work, we analyze the photoactivity of Cu_2O films deposited at different conditions and correlate the photoresponse to morphology, film orientation, and electrical properties. The photoelectrochemical response was measured by linear sweep voltammetry under chopped simulated AM 1.5 illumination. The highest photocurrent obtained was −2.4 mA cm^{-2} at 0.25 V vs RHE for a film thickness of 1.3 μm. This is the highest reported value reached so far for this material in an aqueous electrolyte under AM 1.5 illumination. The optical and electrical properties of the most photoactive electrode were investigated by UV−vis spectroscopy and electrochemical impedance, while the minority carrier lifetime and diffusion length were measured by optical-pump THz-probe spectroscopy.

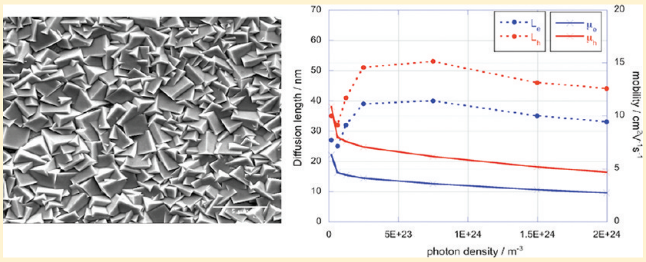

■ INTRODUCTION

Cuprous oxide (Cu_2O) is one of the few oxides that naturally shows p-type conductivity[1−3] and is attractive for solar energy conversion thanks to its direct band gap of 2 eV, which upon integration of the AM1.5 spectrum would correspond to a theoretical photocurrent of 14.7 mA cm^{-2}. In recent years, it has been explored as a photocatalyst for solar-driven water splitting and H_2 generation,[4−11] as an electrode for lithium ion batteries[12−14] and as a p-type semiconductor in junction with n-type ZnO for photovoltaic applications.[15−18]

The p-type character is attributed to Cu vacancies that form acceptor levels several hundred meV above the valence band.[19,20] The hole mobility depends on the preparation method, but values as high as 100 cm^2 V^{-1} s^{-1} have been reported for single crystals,[21] making it attractive from a majority carrier transport perspective.

For solar water splitting, Cu_2O possesses favorable energy band positions, with a predicted flat band potential approximately 0.2 V positive of the hydrogen evolution reaction based on the Mulliken electronegativities of the constituent atoms.[22] There are only a few studies of Cu_2O photocathodes[6,7,9] for hydrogen evolution in the literature, and the measured photocurrents are much smaller than the theoretical maximum, with values typically reported to be less than 1 mA cm^{-2}. Also, the reported photocurrents have been measured with varying illumination intensities and spectral distributions, making comparisons difficult.

The presence of the redox potentials for the reduction and oxidation of Cu_2O within the bandgap, at −0.365 V vs NHE and +0.220 V vs NHE, respectively, has not encouraged the photoelectrochemical investigation of this material in aqueous electrolytes. While single crystal Cu_2O decomposes[23,24] into Cu when used as photocathode in aqueous solution, in some cases electrodeposited polycrystalline Cu_2O has been reported to be stable.[6] This contradictory behavior has been explained[25] in terms of exposed crystal faces, with O^{2-}-terminated faces allowing H^+ species to adsorb and initiate the Cu_2O reduction reaction. The electrodeposited sample reported by De Jongh et al. presented octahedral grains exposing the {111} faces,[6] which can be either Cu^{2+}-terminated or O^{2-}-terminated, and would be more stable if the surface were Cu^{2+}-terminated. The single crystal reported by Takeushi et al. had exposed {211} and {311} faces, which are always O^{2-}-terminated, and therefore photocathodic degradation was observed.

Received: February 6, 2012
Published: March 8, 2012

dx.doi.org/10.1021/jp301176y | *J. Phys. Chem. C* 2012, 116, 7341−7350

We have shown elsewhere[26] that the use of Cu_2O for water splitting or photoelectrochemistry in other H^+-containing environments is possible with the use of a protective nanolayer of a suitable stable oxide without significant losses of photocurrent. The result that Cu_2O can be stabilized motivates us to revisit this characteristically unstable semiconductor in order to improve its photoelectrochemical response in aqueous electrolytes, with the aim of employing this ultra low-cost material for solar fuel production.

Several studies on Cu_2O electrodeposition,[27−31] which is an attractive, robust, and scalable synthesis process, have shown that film morphology and orientation can be tuned by judiciously controlling deposition process parameters, such as: pH, electrolyte bath temperature, and current density or potential. The morphology, nanostructure, and orientation are important to control because they are known to have a dramatic effect on performance in other materials systems such as TiO_2[32] and Fe_2O_3 photoanodes[33] through their role in minority carrier transport to the electrolyte. Despite the body of literature on Cu_2O electrodeposition, no systematic investigation has been carried out relating the deposition parameters to materials properties for photoelectrochemical response.

In this work, the relationship between Cu_2O electrodeposition conditions and photocurrent generation in an aqueous environment was studied by performing experiments at different deposition rates, temperatures, and pH values while keeping constant the total amount of deposited material. These films were then characterized to determine the effect of the synthesis conditions on materials properties. The photocurrent generation in an aqueous electrolyte under AM1.5 illumination was measured for the Cu_2O films synthesized at each condition and then related to the material properties.

EXPERIMENTAL SECTION

Cu_2O Electrodeposition. The Cu_2O thin films were deposited by electrodeposition from a basic solution of lactate-stabilized copper sulfate. The substrate for the electrodeposition (working electrode) was TEC-15 Fluorine-doped tin oxide (FTO, NGS glass) coated with 100 nm of Au, deposited by thermal evaporation atop a 10 nm Cr adhesion layer. Au-coated substrates were chosen over ITO or FTO because both the film thickness and the PEC performances were more reproducible. The plating bath was a 0.2 M $CuSO_4$ (Sigma Aldrich) and 3 M lactic acid (Fisher Scientific) solution in deionized (DI) water with 0.5 M K_2HPO_4 (Sigma Aldrich) buffer. The given concentrations refer to the plating solution before adjusting the bath pH to the desired value by addition of a controlled amount of 2 M KOH. For most depositions, a pH value of 12 was used. In select experiments, deposition was carried out at pH 9. Basic pH values were used to ensure that the Cu_2O was p-type, as it is known that Cu_2O deposited at acidic pH values can exhibit n-type behavior.[34] The temperature of the bath was maintained at 30 or 60 °C using a heating plate with an in situ temperature probe. Above 60 °C, the plating solution became unstable and a black precipitate formed. The Cu_2O thin films were deposited at a constant current density (Galvanostatic mode) using a source-meter (2400, Keithley) in a two electrode configuration (a Pt mesh served as counterelectrode) such that the total charge passed during deposition was the same for every condition, and equal to 1.2 C cm^{-2}. The film thickness was measured by a profileometer (Alpha-step, Tencor). Keeping the total charge passed during deposition constant, the deposition current density was varied in the range from −0.05 to −1.6 mA cm^{-2}. In select experiments, the potential of the working electrode during deposition was measured with respect to an Ag/AgCl reference electrode to assess whether deposition was carried out in the potential window of stability for Cu_2O on the Pourbaix diagram.

Structural and Optical Characterization. The morphology of the films was characterized using a high-resolution scanning electron microscope (FEI XL30 SFEG). X-ray diffraction patterns were acquired with a Bruker D8 Discover diffractometer in Bragg−Brentano mode, using Cu $K\alpha$ radiation (1.540598 Å) and a Ni β-filter. Spectra were acquired with a linear silicon strip "Lynx Eye" detector for $2\theta = 20-80°$ at a scan rate of 3 deg./min., step width 0.02° with source slit width 4 mm. Reflection patterns were matched to the PDF-4+ database (ICDD).

X-ray photoelectron spectroscopy (XPS) data were collected by an Axis Ultra instrument (Kratos analytical, Manchester, UK) under ultrahigh vacuum condition ($<10^{-8}$ Torr) and using a monochromatic Al K_α X-ray source (1486.6 eV), in the Surface Analysis Facility of the Interdisciplinary Centre for Electron Microscopy at EPFL. The source power was maintained at 150 W and the emitted photoelectrons were sampled from a square area of 200 × 200 μm^2. The photoelectron takeoff angle, between the surface and the direction in which the photoelectrons were analyzed, was 90°. The analyzer pass energy was 80 eV for survey spectra and 40 eV for high-resolution spectra. The chemical state of copper being difficult to determine using the Cu 2p binding energy, the Auger Cu LMM signal was also recorded. The adventitious carbon 1s peak was calibrated at 285 eV and used as an internal standard to compensate for any charging effects. Sputtering of the surface by a 3 keV Argon ion beam was used to depth profile the samples with an estimated crater size of 1 × 1 mm^2. The etch rate was approximately 4 nm min^{-1}. Both curve fitting of the spectra and quantification were performed with the CasaXPS software, using relative sensitivity factors given by Kratos.

Transmittance and reflectance spectra were measured with a spectrophotometer Varian Cary 5 equipped with an integrating sphere. The measurements were carried out on a Cu_2O film electrodeposited on a transparent substrate (FTO).

Photoelectrochemical and Electrochemical Impedance Measurements. The photoelectrochemical performance of the electrodes was evaluated in a three-electrode configuration under front-side simulated AM 1.5 illumination using an Ivium Potentiostat/Galvanostat. The electrolyte was a 1.0 M Na_2SO_4 solution buffered at pH 4.9 with potassium phosphate (0.1 M). The reference electrode was Ag/AgCl in saturated KCl, and a Pt wire was used as the counter electrode. The photoresponse was measured under chopped irradiation from a 450 W Xe-lamp (Osram) equipped with a UV filter (KG3 filter, 3 mm, Schott), calibrated with a Si diode in order to simulate AM 1.5 illumination (100 mW cm^{-2}). The scan rate for the linear sweep voltammetry was 10 mV s^{-1}.

The electrochemical impedance measurements were carried out in the dark using an Ivium Potentiostat. The electrolyte was 0.1 M sodium acetate (pH 7.85) in water. The potential was swept in the range of stability predicted by the Pourbaix diagram and an AC signal of 10 mV of amplitude was superposed on the DC component. Before capacitance measurement, the native CuO layer on the surface of the

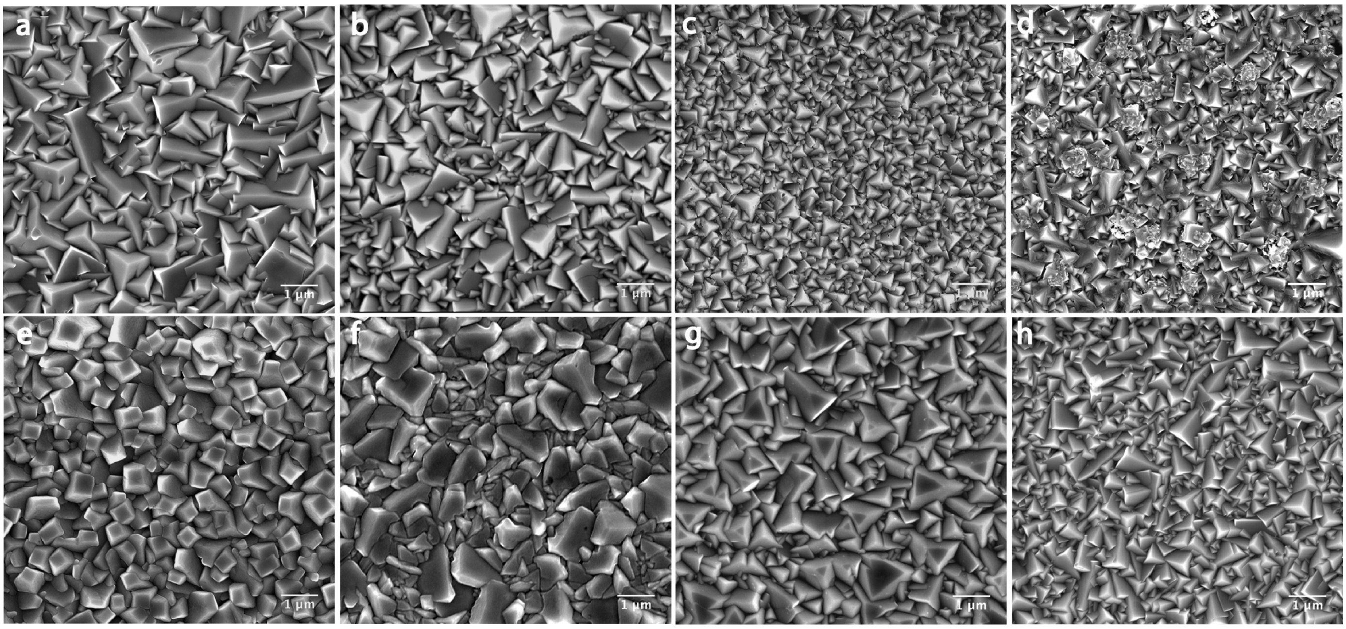

Figure 1. Cu_2O films deposited from the copper lactate solution buffered at pH 12. a−d are micrographs of films deposited at 30 °C for deposition currents of −0.05, − 0.1, − 0.15, − 0.2 mA cm^{-2}, respectively. e−f are micrographs of films deposited at 60 °C for deposition currents of −0.2, − 0.4, − 0.8, − 1.6 mA cm^{-2}, respectively.

electrode was removed by dipping for 15 s in a 0.85 M acetic acid solution.

Optical-Pump THz-Probe Measurements. Optical-pump THz-probe spectroscopy is a purely optical technique to measure charge dynamics on an ultrafast time scale.[35,36] The experimental setup[37] can briefly be described as follows. The initial pulsed laser beam (1 kHz repetition rate, 45 fs pulse duration, 4.5 mJ/pulse energy, λ = 800 nm wavelength) provided by an amplified Ti:Sapphire laser (Coherent Libra USP HE) is split into different paths. Approximately 1.4 mJ/pulse is used to pump an OPerA-Solo optical parametric amplifier (Coherent), which is used as an optical pump to photogenerate carriers in the sample. A second part of the beam with approximately 0.9 mJ/pulse energy is used to generate single cycle THz pulses by optical rectification in a 1 mm-thick ZnTe crystal. The THz beam is focused by gold mirrors on the sample and used as a probe. The transmitted THz pulses are detected in the time-domain through free space electro-optic sampling. A third part of the initial laser beam (0.9 mJ/pulse) is used as a gating beam and guided over a delay line onto a 0.5 mm-thick ZnTe detector crystal. By varying the time delays between the optical pump, the THz probe pulse and the gating, amplitude and phase changes of the THz single-cycle pulses can be recorded. Changes of the amplitude of the THz pulses upon photoexcitation were measured in this work on a time scale of 1 ns with subpicosecond time resolution.

■ RESULTS AND DISCUSSION

For metal oxide semiconductors, performance in photoelectrochemical solar energy conversion applications is often limited by minority carrier transport to the electrolyte interface and the competition between reaction and recombination at the semiconductor surface. The measured photocurrent is a convolution of a number of material properties, such as: surface area, exposed crystal facet, crystallographic orientation, photoexcited electron lifetime, and majority carrier concentration. We seek to control the materials properties important for photocurrent generation through two convenient process parameters: deposition current density and deposition bath temperature. Since these convenient process parameters can simultaneously change a number of properties important for performance, a semiempirical approach is taken where the photocurrent generation is the performance metric. Films were synthesized keeping the total charge passed over the course of deposition constant while changing the deposition current density, or growth rate. The effect of the deposition rate on various materials properties is discussed in this section and correlated to photocurrent generation in the aqueous electrolyte under simulated AM1.5 illumination. The deposition conditions are identified that result in the Cu_2O that produces the highest photocurrent, and these films are chosen for more detailed optoelectronic characterization presented later in the work.

Electrodeposition. The deposition of Cu_2O on Au followed the method developed by Switzer and co-workers.[27] By complexing with lactate ion, Cu^{2+} species are stabilized in the alkaline solution and diffuse in the plating bath to the working electrode surface where they discharge and deposit. The cathodic reduction of cupric lactate to Cu_2O consists of the reduction of Cu^{2+} to Cu^+ followed by the precipitation of Cu^+ as Cu_2O due to the low solubility of monovalent copper in water. The possible reactions that can occur in the reduction of copper lactate are as follows:[38]

$$2Cu^{2+} + H_2O + 2e^- \rightarrow Cu_2O + 2H^+ \tag{1}$$

$$Cu_2O + 2e^- + 2H^+ \rightarrow Cu + H_2O \tag{2}$$

Reactions (1) and (2) are pH dependent and occur in a potential window determined by the potential-pH predominance area diagram, or Pourbaix diagram,[39] for a given temperature.

In electrodeposition either the potential or the current of deposition are controlled and the other variable is allowed to fluctuate. According to the Butler−Volmer equation, the

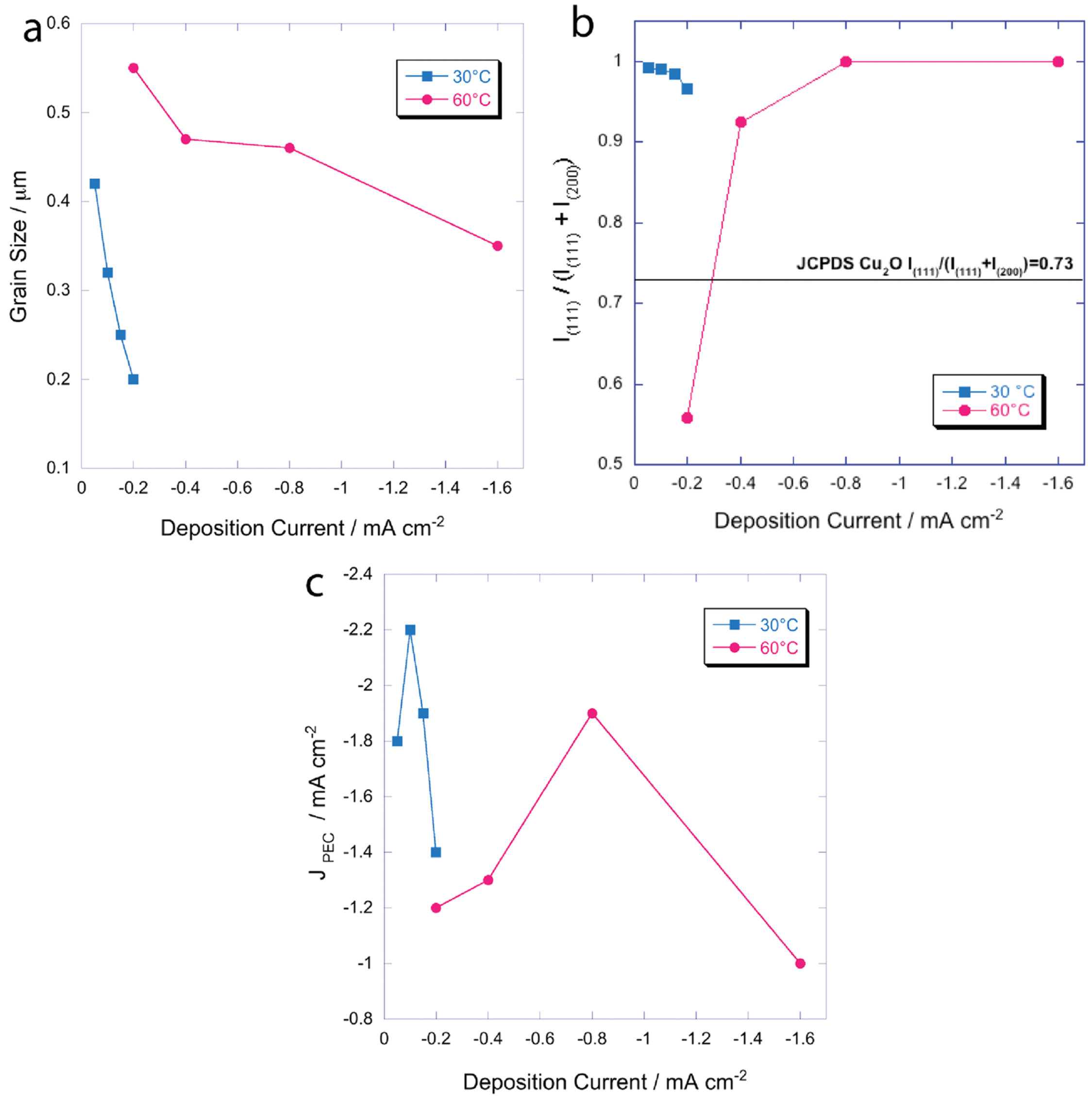

Figure 2. (a) Dependence of morphology on electrodeposition current (or growth rate): average grain sizes of the Cu_2O thin films at different deposition currents for 30 and 60 °C as measured on SEM images. (b) Dependence of orientation on electrodeposition current (or growth rate): plot of intensity $I(111)/ I(111) + I(200)$ of X-ray diffraction peaks as a function of the deposition photocurrent at 30 and 60 °C. (111) and (200) are the main reflections from the deposited films. The line in the graph show the intensities ratio according to the JCPDS card no. 05−0667. (c) Dependence of photoelectrochemical response on electrodeposition current (or growth rate): plot of photoelectrochemical currents measured at 0.25 V vs RHE for Cu_2O thin films grown at different deposition currents.

deposition current depends exponentially on the overpotential, which is the difference between the applied potential and the equilibrium reduction potential of Cu^{2+} to Cu^{+} for a given Cu^{2+} concentration (Nernst equation). Galvanostatic deposition is advantageous from a processing perspective because the film deposition rate can be precisely controlled and the deposit grows linearly with time. For the morphologies illustrated in Figure 1, the pH and temperature (30 or 60 °C) of the deposition bath were fixed and the deposition current was varied. The deposition current controls both the crystal nucleation and the growth rate, which in turn determine the crystal grain size and the film orientation (Figure 2a,b).

The growth rate G follows Faraday's law (3) and is only current-dependent:

$$G = \frac{M \cdot J}{z \cdot \rho \cdot F} \tag{3}$$

where M is the molecular mass and ρ is the bulk density of the deposit, J is the deposition current density, z is the number of electrons exchanged and F is the Faraday constant. It should be noted that eq 3 assumes 100% Faradaic efficiency, that is every measured electron is from the electrochemical reaction of interest. At low deposition currents, crystal growth is slow and grains typically show polyhedral shapes with well-developed facets. The growth rate is limited at high deposition currents by the metal codeposition reaction 2. During galvanostatic Cu_2O deposition, copper metal codeposition is characterized by large oscillations of the electrode potential at fixed current, due to localized pH variations.[40,41] In order to achieve higher growth rates, therefore higher deposition currents, the temperature must be increased. This corresponds to increasing the slope of the phase-boundary lines in the Pourbaix diagram according to the Nernst equation.

For a given deposition rate, if one compares the grain size of the Cu_2O deposited at 30 °C to that deposited at 60 °C, then a larger grain size is observed at the higher deposition temperature (Figures 1 and 2a). At a fixed temperature, a decrease in grain size is observed with higher deposition currents both at 30 °C and at 60 °C (Figures 1 and 2a). Although the same charge was passed for all of the deposited films, those grown at high temperature were thicker than the low-temperature ones; $1.3 \pm 0.1\ \mu m$ at 30 °C and $1.8 \pm 0.1\ \mu m$ at 60 °C.

Our experiments show that both the deposition current and temperature have an effect on the crystallographic orientation, as measured by XRD (Figure 2b). It is known that the grains grow parallel to the surface with the fastest kinetics, while the exposed faces are the surfaces that grow slower[34] and the relative growth rate determines the crystal shape. Also, for a given crystallographic orientation, different exposed facets can be obtained by the addition to the plating bath of species that selectively adsorb on the growing crystal facets.[29,42] The crystallographic orientation is relevant to charge transport and collection, while the exposed facets determine the photocatalytic activity of the films. The black line in Figure 2b shows the ratio between the intensity of the (111) reflection and the sum of the intensities of (111) and (200) reflections for a polycrystalline Cu_2O powder obtained from JCPDS Card No. 05−0667. At 30 °C, a strong (111) orientation was found for all the deposited films, slightly decreasing with increasing deposition current. The (111) oriented grains were cubes with the {100} faces exposed for all the low-temperature depositions, with a reduced crystal size at higher deposition rates (Figure 1a−d). At 60 °C, the crystallographic orientation showed the opposite trend, with (111) orientation reached at higher deposition currents. The crystal shape changed considerably with the deposition current density for the 60 °C samples, from cubooctahedral (Figure 1e), to truncated cubic (Figure 1g) and finally to cubic with the {100} faces exposed (Figure 1h).

Photoelectrochemistry. The film photoactivity as a function of the deposition conditions is shown in Figure 2c. All of the electrodes deposited at pH 12 generated large photocurrents (>1 mA cm^{-2} at 0.25 V vs RHE) under simulated AM 1.5 illumination in the buffered 1 M Na_2SO_4 electrolyte. During the current−potential scan, the illumination was chopped so the dark and the light currents could be simultaneously monitored. There were at least two resulting film properties that changed with the deposition current, resulting in competing factors for determining the photocurrent generated in the aqueous electrolyte. First, as the deposition current approached the potential where Cu_2O was reduced to Cu metal (at higher deposition rates), the semiconductor became copper rich. The presence of copper metal is known to degrade the photoactivity of Cu_2O, which can be readily observed by measuring the stability of Cu_2O under illumination in aqueous electrolytes, where the concentration of Cu metal on the surface increases with time and causes a decrease in photocurrent.[26] Thus, films formed at higher deposition current densities are copper rich and exhibit reduced photoactivity. Deposition currents at which the (111) orientation is maximized are expected to result in better hole collection.[30] For electrodeposited Cu_2O, lower resistivity values have been reported for films with a stronger (111) orientation,[30] where the carrier concentration was higher by almost 2 orders of magnitude for (111)-oriented films when compared to (100)-oriented films and the mobility was approximately the same (1 $cm^2\ V^{-1}\ s^{-1}$) for both orientations, as expected from the isotropic hole effective mass[43,44] and the equal probability of scattering at the grain boundaries.

In Figure 2c, a maximum in the photocurrent as a function of deposition current is observed for both the series of films synthesized at 30 and 60 °C. For the films deposited at 60 °C, the photocurrent increased with (111) orientation until the segregation of Cu occurred (for deposition current of −1.6 mA cm^{-2}). The film grown at −0.8 mA cm^{-2} shows many truncated cubes exposing the triangular (111) faces parallel to the substrate (Figure 1g), which according to Sowers and co-workers[25] are always O^{2-}-terminated, thus prone to H^+-initiated decomposition. A significant contribution to the photocurrent can also come from the exposure of these faces, rather than just the higher (111) orientation. For the film deposited at 30 °C, the decreasing trend in the photocurrent for the deposition currents from −0.1 to −0.2 mA cm^{-2} can also be partially explained by a decrease in the (111) orientation, although relatively small, while it is less clear why the film grown at −0.05 mA cm^{-2} was less photoactive. The lower photocurrent for the film deposited at −0.05 mA cm^{-2} at 30 °C might be explained by the larger grain size and correspondingly lower surface area, as compared to the film deposited at −0.1 mA cm^{-2}, which would result in a longer average minority carrier transport distance to the electrolyte interface and therefore lower collection efficiency, assuming constant lifetime and constant diffusion coefficient. Another possible explanation is that the crystal growth at −0.05 mA cm^{-2} was so close to the equilibrium potential that stoichiometric Cu_2O was produced with a consequently lower hole concentration and higher resistivity.

The best sample deposited at pH 12 generated −2.4 mA cm^{-2} of photocurrent at 0.25 V vs RHE. The corresponding JV plot is presented in Figure 3. The electrodes were not scanned farther than 0.25 V vs RHE because the photocurrent had

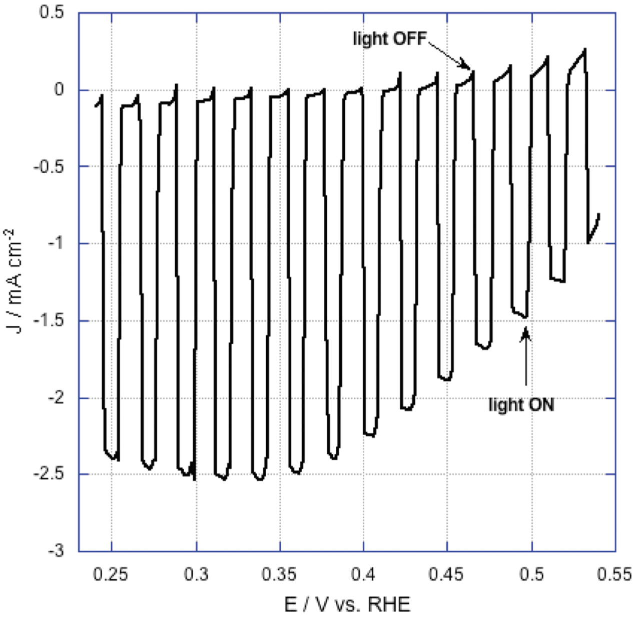

Figure 3. Current−potential characteristic in 1 M Na_2SO_4 solution, under chopped light illumination, for the Cu_2O film grown with −0.1 mA cm^{-2} deposition current, T = 30 °C, pH 12 (our optimal electrodeposition conditions).

already reached the plateau and rapidly decreased at more cathodic potentials due to the dark reaction of metal oxide reduction.

The photocurrents obtained in this study were considerably larger than those previously reported for electrodeposited Cu_2O. One might expect that the unusually high photocurrents are a result of unintentional doping from impurities in the deposition bath. Since sulfur has been found in the Cu_2O electrodeposited at pH 12,[45] likely coming form the sulfate, unintentional doping in our Cu_2O films was investigated using XPS by collecting spectra at different depths below the surface for a sample deposited at the conditions that produced the highest photocurrent. The XPS analysis showed only signals from Cu and O and there was no evidence of sulfur, phosphorus or carbon inclusion from the sulfate, phosphate, or lactate in the deposition bath.

The measured photocurrents for the bare Cu_2O contained large contributions from reduction of the semiconductor to Cu metal, which was visually observed by the formation of a black circle where the electrode was illuminated and also by SEM images that revealed Cu nanoparticles on the surface of the Cu_2O grains (Figure S4 of the SI).

On the kinetics of the Cu_2O reduction reaction at the surface, a significant factor is the availability of surface oxygen in the solid phase and the Cu^+ coordination number. Both {100} and {111} planes are either O-layers or Cu-layers, but the stoichiometric Cu_2O (111) surface is not polar[46] while the Cu_2O (100) surface is polar[46] and can favor H^+-adsorption and Cu_2O decomposition through reaction 2.

All of the Cu_2O electrodes used in this study, regardless of the synthesis conditions, potential and pH at which the PEC characterization was performed (both inside and outside the predominance area of the Pourbaix diagram) or crystallographic orientation, showed black spots where they were illuminated indicating reduction to Cu metal, although the black spots appeared at different rates. Even samples deposited at pH 9, which had a stronger (200) orientation and predominantly exposed {111} planes (Figure S2a,c of the SI), eventually turned black, although at a much slower rate (and correspondingly lower photocurrent) than the (111) oriented samples. Figure S4 of the SI shows an SEM image of an electrode after PEC measurement. Cu LMM Auger spectra in XPS were also collected to resolve the chemical information immediately below the surface, and evidence of Cu_2O reduction was found from the shift of Cu LMM signal position from a kinetic energy of 917.4 eV in the pristine sample toward higher kinetic energies after the PEC characterization (Figure S6 of the SI), which indicates the presence of metallic copper in the latter case.

With an understanding of how the deposition conditions affect the materials properties and photocurrent generation, we next seek to provide a picture of the critical optoelectronic properties of the most active photoelectrode.

Photocurrent generation in metal oxide semiconductors is often limited by minority carrier transport to the semiconductor-electrolyte interface (SEI). For illumination through the electrolyte to a planar semiconductor junction, the photons are absorbed and the intensity in the beam drops exponentially with distance in the semiconductor. The depth at which the beam reaches e^{-1} of its initial value is the absorption depth (α^{-1}), which is the characteristic length of light absorption. For a p-type semiconductor, there is an electric field in the semiconductor near the SEI caused by potential-dependent charge depletion that causes band bending, which transports photoexcited electrons to the surface, and holes into the bulk. Typically, all electrons that diffuse to, or are generated in, this depletion region are assumed to be collected. The depletion region has a characteristic length called the space charge layer thickness, which is an estimate of the distance the depletion region extends into the semiconductor. In the ideal case, electrons are collected over a distance equal to the sum of the diffusion distance and space charge layer thickness, which can be called the collection distance. The challenge is that the collection distance is often much shorter than the absorption depth, meaning that for a planar junction only a fraction of the photoexcited carriers are collected. In such a situation where the absorption depth and minority carrier collection distance are incommensurate, nanostructured geometries must be employed to decouple light absorption from minority carrier transport.[47−49] However, before attempting to synthesize such a nanostructured electrode, we first seek to measure the important characteristic length scales in our most photoactive electrodes (−0.1 mA cm^{-2}, T = 30 °C, pH = 12). The absorption depth was determined by UV−visible spectroscopy for a film of known thickness. For the Schottky junction formed in the semiconductor at the SEI, the space charge layer thickness is a function of the electrode potential, flat band potential and majority carrier concentration; which we estimate by impedance analysis and bulk resistivity. Finally, the minority carrier diffusion distance is estimated by ultrafast optical-pump THz-probe measurements.

Optical Properties. The transmittance and reflectance spectra of a Cu_2O film electrodeposited on FTO at −0.1 mA cm^{-2}, T = 30 °C, pH 12, were used to calculate the absorption coefficient spectra of Figure 4 with eq 4:

$$\alpha = \frac{-\ln\left(\frac{T}{1-R}\right)}{d} \tag{4}$$

where d is the sample thickness, T is the transmittance, and R is the reflectance. The Tauc plot (Figure 4) shows an optical band gap of 2.07 eV. At λ = 620 nm, the light penetration depth is

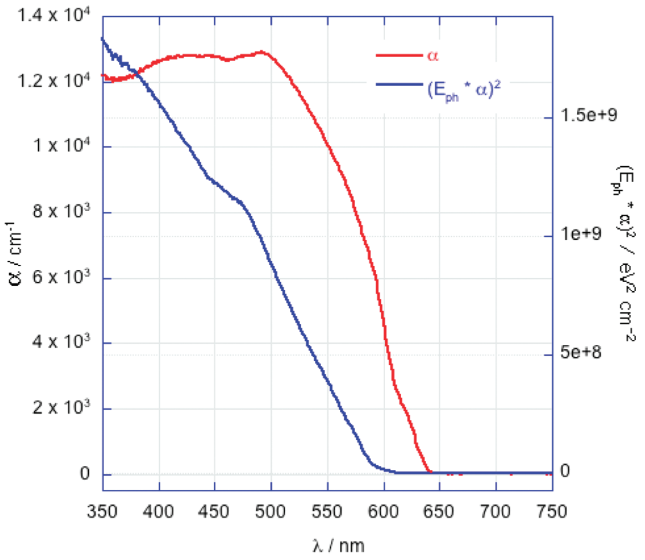

Figure 4. Absorption coefficient and Tauc plot for the most photoactive Cu_2O film.

5.2 μm; α^{-1}(600 nm) = 2.2 μm; α^{-1}(550 nm) = 1.0 μm and α^{-1}(500 nm) = 0.8 μm. Since Au increased reflection from the substrate for $\lambda > 550$ nm, for the Cu_2O-film thickness of this study the use of an Au-coated substrate was a convenient choice. We do note however, that similar photocurrents could be obtained on FTO and ITO substrates but the reproducibility was worse.

Electrochemical Impedance. The most photoactive electrode (−0.1 mA cm^{-2}, T = 30 °C, pH = 12) was characterized by electrochemical impedance spectroscopy in order to determine its flat band potential and estimate the intrinsic acceptor density in the near-surface region. A mild etching in acetic acid was performed before impedance to obtain a fresh Cu_2O surface because XPS showed the existence of a native CuO layer on the electrode surface (Figure S5 of the SI). The frequency scan at fixed potentials produced characteristic semicircles in the Nyquist plot, which indicated that the semiconductor/electrolyte interface can be electrically described by an equivalent circuit of a resistor and a capacitor in parallel. To obtain the Mott−Schottky plots of Figure 5, a potential sweep at fixed frequencies was performed, and the space charge capacitance of the semiconductor could be obtained from the imaginary part of the impedance. The linear data fit allows one to extrapolate the flat band potential and the slope of the linear fit is an estimation of the majority charge carrier concentration, according to the Mott−Schottky eq 5:

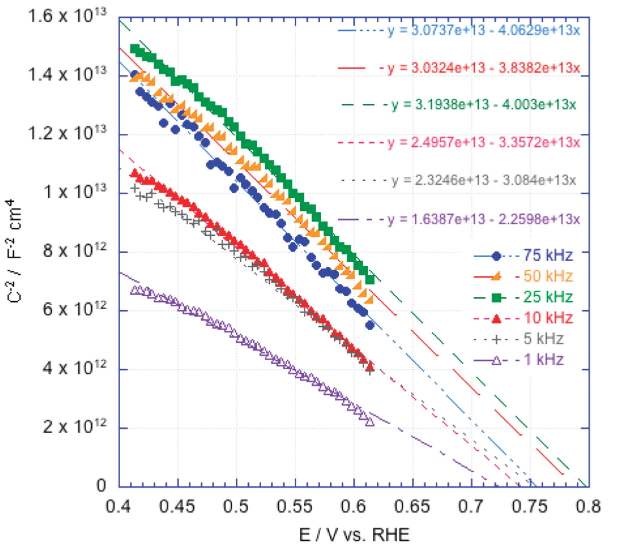

Figure 5. Mott−Schottky plot for the most photoactive Cu_2O film (electrodeposited at −0.1 mA cm^{-2}, 30 °C, pH 12) from electrochemical impedance analysis in 0.1 M sodium acetate (pH 7.85) in water in the dark. The electrode was scanned at fixed frequencies in the potential range of chemical stability.

$$\frac{1}{C^2} = \frac{2}{e\varepsilon\varepsilon_0 N_A}\left(E - E_{fb} - \frac{kT}{e}\right) \tag{5}$$

The measured flat band potential was +0.75 ± 0.05 V/RHE and the carrier concentration calculated from the slopes at higher frequencies (25−75 kHz) was approximately 5 × 10^{17} cm^{-3} using $\varepsilon_{r(\infty)} = 6.6$.[50] This acceptor concentration places the Fermi level 80 meV above the valence band, according to eq 6:

$$E_F - E_{VB} = kT\ln\frac{N_V}{N_A} \tag{6}$$

The effective density of states at the top of the valence band, N_v, was calculated with an effective hole mass of 0.58 m_0.[51] It follows that, for a bandgap value of 2.0 eV, the valence band and the conduction bands are positioned at 0.83 and −1.17 V vs RHE, respectively. The conduction band position is more cathodic than the previously reported by De Jongh[6] to be −0.7 V vs RHE, although the latter refers to Cu_2O electrodeposited in different conditions. It has also been reported[52] that the flat band potential spans a 500-mV range for variations in electrodeposition bath pH by from 9 to 12.

Electrical Resistivity. The bulk acceptor concentration could not be measured directly by Hall effect measurement because of the high sample resistance, even for thicker Cu_2O films (∼5 μm). To perform electrical measurements the electrodeposited Cu_2O was lifted off the conductive substrate with epoxy resin.[30] The measured resistivity (Van-der-Pauw configuration) was 2.0 × 10^5 Ω·cm in the dark. Incidentally, a strong photoconductivity was observed, with the resistivity decreasing by orders of magnitude when the sample was exposed to light, and this phenomenon can explain the good PEC performance in AM 1.5 illumination (Figure 3), despite the high sample resistance. Since no discontinuities in the lift-off samples were observed by SEM, the measured resistivity reveals a much lower acceptor density than that determined from the Mott−Schottky plot. We propose several possible explanations. First, the resistivity can vary with crystallographic direction. The Van der Pauw geometry measures the resistivity of the plane parallel to the substrate, while the Mott−Schottky analysis measures the acceptor concentration in the proximity of the SEI. Second, the intrinsic doping of the electrodeposited Cu_2O can differ from the acceptor concentration obtained from the capacitance of the space-charge layer if there is a stoichiometric gradient from the bulk to the surface. Namely, if the stoichiometry varies from Cu_2O in the bulk to $Cu_{2-x}O$ at the surface, then it is reasonable that the surface acceptor concentration would be higher than the bulk. Assuming a hole mobility of 5 cm^{2}V^{-1}s^{-1} (see THz spectroscopy section below), the hole concentration in the bulk would be in the order of 10^{13} cm^{-3}, as calculated from the Van-der-Pauw resistivity. This value is 4 orders of magnitude lower than what was calculated for the semiconductor surface from the slope of the Mott−Schottky plot, and would place the Fermi level of the bulk at 360 meV above the valence band (eq 6). The question of surface versus bulk properties of Cu_2O is not new in the literature and it has been reported that high bulk resistivity samples, such as those of this study, are not homogeneous from the surface to the bulk and the relatively low resistivity surface layer may vary with exposure to atmosphere, temperature, measurement environment, and so on.[53] A tentative energy level diagram for the semiconductor-electrolyte interface in the dark is presented in Figure S7 of the SI. Given this depth-dependent Fermi level, the equilibration of the Fermi level in the semiconductor builds up an energy barrier for the electron flow from the bulk to the surface of 0.28 eV. Removing this barrier could help to reduce the amount of electrical energy input needed when these electrodes are used for photoelectrochemical water reduction.

THz Spectroscopy. The photoconductivity dynamics were probed in transmission geometry for a 4.35 μm-thick Cu_2O film transferred onto an epoxy substrate at 20 °C and under normal pressure. The sample was excited at 600 and 550 nm with excitation fluences ranging from 1.6 to 211 μJ cm^{-2} resulting in photogenerated charge carrier densities from 1.9 × 10^{16} cm^{-3}

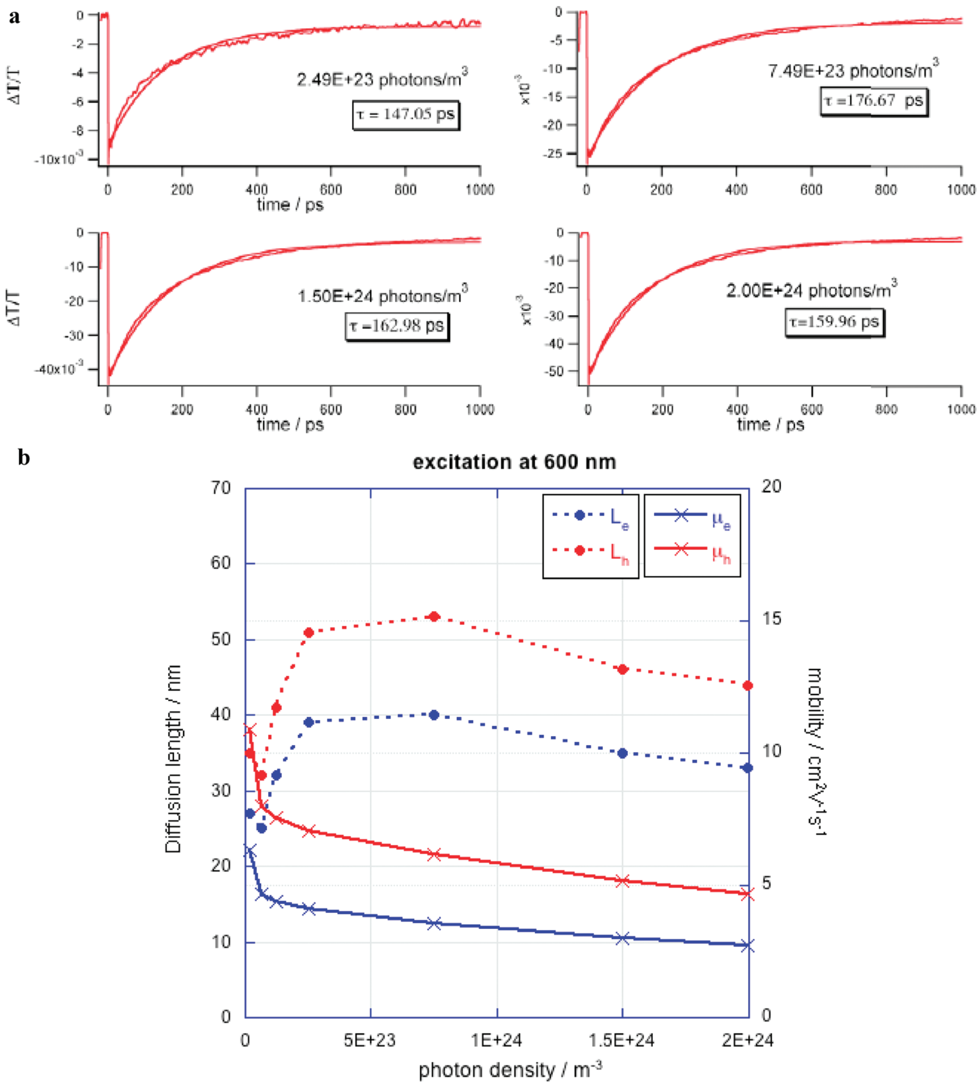

Figure 6. (a) Change in THz transmission when the Cu_2O sample is excited at 600 nm. The experimental data can be fitted by a single exponential, whose time constant depends on the energy of the excitation pulse. (b) Diffusion length and mobility values for holes and electrons calculated from the photoconductivity and time constant values.

to 4.9×10^{18} cm^{-3}. For all scans, a resolution-limited rise time of 500 fs is observed. For excitation at 550 nm, a rapid cooling of the generated charge carriers to the band edge is observed which happens within the first two picoseconds, while upon excitation close to the bandgap, at 600 nm, no fast cooling is observed. On the longer time scale, a decay of the signal is observed that can be fitted quite well by a single exponential. On the shorter time scale, the decay appears only slightly faster. It has to be noted that the time constant is fluence dependent and time constants ranging from ~40 to 176 ps have been measured. Figure 6a shows the photoconductivity dynamics for excitation at 600 nm at different fluences. The faster recombination at low fluence can be explained by recombination at impurity/trap sides, which become saturated for higher charge densities. For the highest probed fluences, the time constant decreases again due to the high charge carrier density. The change in the transmitted THz amplitude ΔT can be related to the photoconductivity $\Delta\sigma$ using eq 7:[54]

$$\Delta\sigma(t) = -\frac{(n_1 + n_2)\varepsilon_0 c}{d}\cdot\frac{\Delta T(t)}{T(t)} \qquad (7)$$

Here, n_1 and n_2 are the refractive indexes of the materials on the frontside and backside of the photoexcited material (in this case air and non-excited copper oxide), c the speed of light, ε_0 the free space permittivity, and d the thickness of the photoexcited material, 2.2 μm for excitation at 600 nm and 1 μm for excitation at 550 nm. It is important to note that this equation is valid for negligibly small phase changes and that the true conductivity is a function of optical penetration depth, whereas the conductivity calculated by using eq 7 is an average value over space and over the accessible frequency range ~0.2−3 THz. Charge mobilities were extracted using relation 8 at times shortly after excitation and hot carrier cooling, but before any decrease of the conductivity due to trapping or recombination of the electron−hole pairs could take place.[55]

$$\varphi\mu = \frac{\Delta\sigma}{efN} \qquad (8)$$

Here ϕ is the charge generation efficiency, e the elementary charge, f the fraction of photons absorbed by the sample and N the incident photon density. The charge generation efficiency has been assumed to be 2 since each absorbed photon leads to the generation of two charge carriers, an electron and a hole. From eqs 7 and 8, the mobility of the charge carriers has estimated at a time ~10 ps after excitation, before any trapping or recombination occurs. Equation 8 takes into account that an electron hole pair is created per absorbed photon and average mobilities in between ~3.6 and 8.5 $cm^2 V^{-1} s^{-1}$ are found for these charge carriers. From the average mobilities of the carriers, we have estimated individual mobilities of the holes and electrons by assuming proportionality to the inverse of the effective mass. Given an effective mass of of 0.58 and 0.99 m_0 for holes and electrons, respectively,[51] and assuming that the scattering rate is similar for the holes and the electrons, the individual mobilities are estimated to be in between 4.6 and 12.8 $cm^2V^{-1}s^{-1}$ for the holes and 2.7–6.3 $cm^2 V^{-1} s^{-1}$ for the electrons. From the mobility, the diffusivity and the diffusion length can be calculated by the relations 9 and 10,

$$D = \frac{kT}{q}\mu \tag{9}$$

$$L = \sqrt{D\cdot\tau} \tag{10}$$

where k is the Boltzmann constant and q the elementary charge, and τ is the electron lifetime. Figure 6b shows the electron and hole diffusion lengths and mobilities obtained at different fluences for excitation at 600 nm. A similar trend with just slightly higher values was found upon sample excitation at 550 nm. The electron diffusion length in the plane parallel to the substrate is found to be between 25 and 60 nm under the probed conditions. This value is smaller than the previously reported value of 160 nm[56] for electrodeposited Cu_2O, which was based on the application of the Gärtner model.

These results provide insight into how to proceed with Cu_2O as an absorber for photoelectrochemical water splitting. If we assume for simplicity that minority carriers (photoexcited electrons) are collected over a distance equal to the sum of the space charge layer thickness (28 nm at 0.25 V vs RHE) and the electron diffusion length (25–60 nm), then the collection distance for electrons (53–88 nm) is clearly not commensurate with the measured absorption depth for photons at the band gap (2.2 μm). For these optimized electrodeposited Cu_2O films, aspect ratios of 10 to 50 will be required to generate the ideal photocurrent of 14.7 mA cm^{-2} under AM1.5 illumination. One hypothetically attractive geometry would be oriented Cu_2O nanowires 50 to 150 nm in diameter and optically thick. Such a structure would require a protective surface layer catalytically activated toward water reduction for solar hydrogen production.

■ CONCLUSIONS

In this work, we have shown that the photoactivity of cuprous oxide can be optimized through judiciously controlling the parameters of electrodeposition and measuring the resulting photocurrent. We found that at pH 12 the Cu_2O films deposited at low temperature were more photoactive than the films deposited at high temperature. At higher temperature, the trend in photocurrent seems to be associated with the (111) orientation, until the deposition current is high enough so Cu metal precipitation occurs, which then decreases the photocurrent. The film morphology shows a stronger dependence on the deposition current at higher temperature. The bath pH is important for controlling the grain shape. The films deposited at pH 9 exhibit lower photoactivity than those deposited at pH 12, which correlated to exposed {111} faces at pH 9 and exposed {100} faces at pH 12. This study also shed light on the issue of Cu_2O instability, which was observed for both the (111) and (100)-oriented films. The best performing Cu_2O film was also optically, electrically, and photoelectrochemically characterized. The highest photocurrent measured so far under AM 1.5 illumination in an aqueous electrolyte for this material was measured, but the challenge of the stability of the Cu_2O surface must be addressed to photoelectrochemically reduce H_2O to H_2.

■ ASSOCIATED CONTENT

Ⓢ Supporting Information

This material is available free of charge via the Internet at http://pubs.acs.org.

■ AUTHOR INFORMATION

Corresponding Author

*E-mail: adriana.paracchino@epfl.ch.

Notes

The authors declare no competing financial interest.

■ ACKNOWLEDGMENTS

We thank the European Commission (Project NanoPEC—Nanostructured Photoelectrodes for Energy Conversion, Contract No. 227179), Swiss Federal Office for Energy (PECHouse Competence Center, Contract No. 152933), and the Energy Center at EPFL, the SNF and NCCR MUST for financial support. We also acknowledge Dr. Vincent Laporte and Nicolas Xanthopoulos from Centre Interdisciplinaire de Microscopie Electronique (CIME) at EPFL for helping in the XPS characterization. A.P. is grateful to Nripan Mathews for reading the manuscript and providing constructive feedback.

■ REFERENCES

(1) Toth, S.; R., K.; Trivich, D. *J. Appl. Phys.* **1960**, *31*, 1117.

(2) Young, A. P.; Schwartz, C. M. *J. Phys. Chem. Solids* **1969**, *30* (2), 249–252.

(3) O'Keeffe, M.; Moore, W. J. *Electrical Conductivity of Monocrystalline Cuprous Oxide*: AIP: College Park, MD, 1961; Vol. 35, p 1324–1328.

(4) Somasundaram, S.; Chenthamarakshan, C. R. N.; de Tacconi, N. R.; Rajeshwar, K. *Int. J. Hydrogen Energy* **2007**, *32* (18), 4661–4669.

(5) Hara, M.; Kondo, T.; Komoda, M.; Ikeda, S.; Shinohara, K.; Tanaka, A.; Kondo, J. N.; Domen, K. *Chem. Commun.* **1998**, *3*, 357–358.

(6) de Jongh, P. E.; Vanmaekelbergh, D.; Kelly, J. J. *J. Electrochem. Soc.* **2000**, *147* (2), 486–489.

(7) Siripala, W.; Ivanovskaya, A.; Jaramillo, T. F.; Baeck, S. H.; McFarland, E. W. *Sol. Energy Mater. Sol. Cells* **2003**, *77* (3), 229–237.

(8) Hu, C. C.; Nian, J. N.; Teng, H. *Sol. Energy Mater. Sol. Cells* **2008**, *92* (9), 1071–1076.

(9) Nian, J. N.; Hu, C. C.; Teng, H. *Int. J. Hydrogen Energy* **2008**, *33* (12), 2897–2903.

(10) Barreca, D.; Fornasiero, P.; Gasparotto, A.; Gombac, V.; Maccato, C.; Montini, T.; Tondello, E. *Chemsuschem* **2009**, *2* (3), 230–233.

(11) Wu, L. L.; Tsui, L. K.; Swami, N.; Zangari, G. *J. Phys. Chem. C* **2010**, *114* (26), 11551–11556.

(12) Morales, J.; Sanchez, L.; Bijani, S.; Martinez, L.; Gabas, M.; Ramos-Barrado, J. R. *Electrochem. Solid State Lett.* **2005**, *8* (3), A159–A162.

(13) Lee, Y. H.; Leu, I. C.; Liao, C. L.; Chang, S. T.; Wu, M. T.; Yen, J. H.; Fung, K. Z. *Electrochem. Solid State Lett.* **2006**, *9* (4), A207–A210.

(14) Bijani, S.; Gabas, M.; Martinez, L.; Ramos-Barrado, J. R.; Morales, J.; Sanchez, L. *Thin Solid Films* **2007**, *515* (13), 5505−5511.
(15) Katayama, J.; Ito, K.; Matsuoka, M.; Tamaki, J. *J. Appl. Electrochem.* **2004**, *34* (7), 687−692.
(16) Akimoto, K.; Ishizuka, S.; Yanagita, M.; Nawa, Y.; Paul, G. K.; Sakurai, T. *Solar Energy* **2006**, *80* (6), 715−722.
(17) Jeong, S. S.; Mittiga, A.; Salza, E.; Masci, A.; Passerini, S. *Electrochim. Acta* **2008**, *53* (5), 2226−2231.
(18) Cui, J. B.; Gibson, U. J. *J. Phys. Chem. C* **2010**, *114* (14), 6408−6412.
(19) Paul, G. K.; Nawa, Y.; Sato, H.; Sakurai, T.; Akimoto, K. *Appl. Phys. Lett.* **2006**, *88* (14), 141901.
(20) Scanlon, D. O.; Morgan, B. J.; Watson, G. W.; Walsh, A. *Phys. Rev. Lett.* **2009**, *103* (9), 096405.
(21) Fortin, E.; Weichman, F. L. *Can. J. Phys.* **1966**, *44* (7), 1551-&.
(22) Osterloh, F. E. *Chem. Mater.* **2008**, *20* (1), 35−54.
(23) Gerischer, H. *J. Electroanal. Chem. Interfacial Electrochem.* **1977**, *82*, 133.
(24) Takeuchi, M.; Weichman, F. L.; Morosawa, K.; Kawakami, M.; Nagasaka, H. *Appl. Surf. Sci.* **1988**, *33*−*4*, 972−979.
(25) Sowers, K. L.; Fillinger, A. *J. Electrochem. Soc.* **2009**, *156* (5), F80−F85.
(26) Paracchino, A.; Laporte, V.; Sivula, K.; Grätzel, M.; Thimsen, E. *Nat. Mater.* **2011**, *10* (6), 456−461.
(27) Golden, T. D.; Shumsky, M. G.; Zhou, Y. C.; VanderWerf, R. A.; VanLeeuwen, R. A.; Switzer, J. A. *Chem. Mater.* **1996**, *8* (10), 2499−2504.
(28) Mahalingam, T.; Chitra, J. S. P.; Rajendran, S.; Jayachandran, M.; Chockalingam, M. J. *J. Cryst. Growth* **2000**, *216* (1−4), 304−310.
(29) Siegfried, M. J.; Choi, K. S. *Angew. Chem., Int. Ed.* **2005**, *44* (21), 3218−3223.
(30) Mizuno, K.; Izaki, M.; Murase, K.; Shinagawa, T.; Chigane, M.; Inaba, M.; Tasaka, A.; Awakura, Y. *J. Electrochem. Soc.* **2005**, *152* (4), C179−C182.
(31) Bijani, S.; Martinez, L.; Gabas, M.; Dalchiele, E. A.; Ramos-Barrado, J. R. *J. Phys. Chem. C* **2009**, *113* (45), 19482−19487.
(32) Thimsen, E.; Rastgar, N.; Biswas, P. *J. Phys. Chem. C* **2008**, *112* (11), 4134−4140.
(33) Cesar, I.; Sivula, K.; Kay, A.; Zboril, R.; Graetzel, M. *J. Phys. Chem. C* **2009**, *113* (2), 772−782.
(34) Wang, L. C.; Tao, M. *Electrochem. Solid State Lett.* **2007**, *10* (9), H248−H250.
(35) Schmuttenmaer, C. A. *Chem. Rev.* **2004**, *104* (4), 1759−1779.
(36) Nemec, H.; Kuzel, P.; Sundstrom, V. *J. Photochem. Photobiol. A-Chem.* **2010**, *215* (2−3), 123−139.
(37) Brauer, J. C.; Thorsmolle, V. K.; Moser, J. E. *Chimia* **2009**, *63* (4), 189−192.
(38) Zhou, Y. C.; Switzer, J. A. *Mater. Res. Innovat.* **1998**, *2*, 22−27.
(39) Pourbaix, M. *Atlas of Electrochemical Equilibria in Aqueous Solutions, NACE* 1974.
(40) Leopold, S.; Herranen, M.; Carlsson, J. O. *J. Electrochem. Soc.* **2001**, *148* (8), 513−517.
(41) Neogi, P. *J. Chem. Phys.* **2004**, *121* (19), 9630−9638.
(42) Choi, K. S. *Dalton Trans.* **2008**, 5432−5438.
(43) Nie, X.; Wei, S.-H.; Zhang, S. B. *Phys. Rev. B* **2002**, *65* (7), 075111.
(44) Ohyama, T.; Ogawa, T.; Nakata, H. *Phys. Rev. B* **1997**, *56* (7), 3871.
(45) Nadesalingam, M. P.; Mukherjee, S.; Somasundaram, S.; Chenthamarakshan, C. R.; de Tacconi, N. R.; Rajeshwar, K.; Weiss, A. H. *Langmuir* **2007**, *23* (4), 1830−1834.
(46) Schulz, K. H.; Cox, D. F. *Phys. Rev. B* **1991**, *43* (2), 1610.
(47) Lin, Y.; Yuan, G.; Sheehan, S.; Zhou, S.; Wang, D. *Energy Environ. Sci.*
(48) Spurgeon, J. M.; Atwater, H. A.; Lewis, N. S. *J. Phys. Chem. C* **2008**, *112* (15), 6186−6193.
(49) Kayes, B. M.; Atwater, H. A.; Lewis, N. S. *J. Appl. Phys.* **2005**, *97*, 11.
(50) Heltemes, E. C. *Phys. Rev.* **1966**, *141* (2), 803.
(51) Hodby, J. W.; Jenkins, T. E.; Schwab, C.; Tamura, H.; Trivich, D. *J. Phys. C-Solid State Phys.* **1976**, *9* (8), 1429−1439.
(52) Wang, L. C.; de Tacconi, N. R.; Chenthamarakshan, C. R.; Rajeshwar, K.; Tao, M. *Thin Solid Films* **2007**, *515* (5), 3090−3095.
(53) Fortin, E.; Rochon, P.; Zielinger, J. P. *J. Phys. Chem. Solids* **1975**, *36* (11), 1299−1306.
(54) Nienhuys, H. K.; Sundstrom, V. *Phys. Rev. B* **2005**, *71*, 23.
(55) Snaith, H. J.; Tiwana, P.; Parkinson, P.; Johnston, M. B.; Herz, L. M. *J. Phys. Chem. C* **2010**, *114* (2), 1365−1371.
(56) Liu, Y. C.; Turley, H. K.; Tumbleston, J. R.; Samulski, E. T.; Lopez, R. *Appl. Phys. Lett.* **2011**, *98*, 16.